# OPTICAL-FLOW FOR 3D ATMOSPHERIC MOTION ESTIMATION

Patrick Héas and Etienne Mémin
*INRIA - IRISA, Campus de Beaulieu, Rennes, France*

Keywords: 3D Motion estimation, Variational methods, Optical-flow, Atmospheric dynamics, Physical-based model.

Abstract: In this paper, we address the problem of estimating three-dimensional motions of a stratified atmosphere from satellite image sequences. The complexity of three-dimensional atmospheric fluid flows associated to incomplete observation of atmospheric layers due to the sparsity of cloud systems makes very difficult the estimation of dense atmospheric motion field from satellite images sequences. The recovery of the vertical component of fluid motion from a monocular sequence of image observations is a very challenging problem for which no solution exists in the literature. Based on a physically sound vertical decomposition of the atmosphere into layers of different altitudes, we propose here a dense motion estimator dedicated to the extraction of three-dimensional wind fields characterizing the dynamics of a layered atmosphere. Wind estimation is performed over the complete three-dimensional space using a multi-layer model describing a stack of dynamic horizontal layers of evolving thickness, interacting at their boundaries via vertical winds. The efficiency of our approach is demonstrated on synthetic and real sequences.

## 1 INTRODUCTION

Geophysical motion characterization and analysis by image sequence analysis is a crucial issue for numerous scientific domains involved in the study of climate change, weather forecasting, climate prediction or biosphere analysis. The use of surface station, balloon, and more recently in-flight aircraft measurements and low resolution satellite images has improved the estimation of wind fields and has been a subsequent step for a better understanding of meteorological phenomena. However, the network's temporal and spatial resolutions may be insufficient for the analysis of mesoscale dynamics. Recently, in an effort to avoid these limitations, another generation of satellites sensors has been designed, providing image sequences characterized by finer spatial and temporal resolutions. Nevertheless, the analysis of motion remains particularly challenging due to the complexity of atmospheric dynamics at such scales.

Tools are needed to exploit this new generation of satellite images and we believe that it is very important that the computer vision community gets involved in such domain as they can potentially bring relevant contributions with respect to the analysis of spatio-temporal data.

Nevertheless in the context of geophysical motion analysis, standard techniques from Computer Vision, originally designed for bi-dimensional quasi-rigid motions with stable salient features, appear to be not well adapted (Horn and Schunck, 1981) (Leese et al., 1971). The design of techniques dedicated to fluid flow has been a step forward, towards the constitution of reliable methods to extract characteristic features of flows (Anonymous)(Anonymous)(Zhou et al., 2000). However, for geophysical applications, existing fluid-dedicated methods are all limited to horizontal velocity estimation and neglect vertical motion. All these methods are obviously not adapted to the extraction of 3D measurements but also do not take into account accurately luminance variations due to 3D motions. Such effects are occasionally important at small scales and should be incorporated in the motion estimation method.

Geophysical flows are quite well described by appropriate physical models. As a consequence in such contexts, a physically-based approach can be very powerful for analyzing incomplete and noisy image data, in comparison to standard statistical methods. The inclusion of physical *a priori* leads to novel advanced techniques for motion analysis or 3D information recovery. This yields to new application domains



Héas P. and Mémin E. (2008).
OPTICAL-FLOW FOR 3D ATMOSPHERIC MOTION ESTIMATION.
In *Proceedings of the Third International Conference on Computer Vision Theory and Applications*, pages 399-406
DOI: 10.5220/0001071503990406

impacting potentially studies of capital interest for our everyday life, and obviously to the devise of proper efficient techniques. This is thus a research domain with wide perspectives. Our work is a contribution towards this direction.

The method proposed in this paper is significantly different from previous works on motion analysis by satellite imagery. A main difference is that the data model used in our method relies on an exact 3D physical model for pressure difference image observations retrieved at different atmospheric levels. This interacting layered model allows us to recover a vertical motion information.

## 2 RELATED WORKS ON OPTICAL FLOW

The problem of wind field recovery consists in estimating the 3D atmospheric motion denoted by $\mathbf{V}(\mathbf{s},t)$ from a 2D image sequence $I(\mathbf{s},t)$, where $(\mathbf{s},t)$ denote the pixel and time coordinates. This problem is a complex one, for which we have only access to projected information on clouds position and spectral signatures provided by satellite observation channels. To avoid the three-dimensional wind field reconstruction problem, all developed methods have relied on the assumption of negligible vertical winds and focused on the estimation of a global apparent horizontal winds related to top of clouds of different heights.

The estimation of the apparent motion $\mathbf{v}(\mathbf{s},t)$ as perceived through image intensity variations (the so-called optical-flow) relies principally on the temporal conservation of some invariants. The most common invariant used is the brightness constancy assumption. This assumption leads to the well known Optical-Flow Constraint (OFC) equation

$$\mathbf{v}\cdot\nabla I(\mathbf{s},t)+I_t(\mathbf{s},t)=0 \tag{1}$$

An important remark is that for image sequences showing evolving atmospheric phenomena, the brightness consistency assumption does not allow to model temporal distortions of luminance patterns caused by 3D flow transportation. In spite of that, most estimation methods used in the meteorology community still rely on this crude assumption (Larsen et al., 1998). In the case of transmittance imagery, the Integrated Continuity Equation (ICE) provides a valid invariant assumption for compressible flows (Fitzpatrick, 1988) under the assumption that the temporal derivatives of the integration boundaries compensate the normal flows. This ICE model reads :

$$\Big(\int \rho dz\Big)_t+\mathbf{v}.\nabla\Big(\int \rho dz\Big)+\Big(\int \rho dz\Big)\mathrm{div}\mathbf{v}=0 \tag{2}$$

where $\rho$ and $\mathbf{v}$ denote the fluid density and the density averaged horizontal motion field along the vertical axis. Unlike the OFC, such models can compensates mass departures observed in the image plan by associating two-dimensional divergence to brightness variations. But, for the case of satellite infra-red imagery, the assumption that $I\propto\int\rho dz$ is flawed. Moreover, note that although the assumed boundary condition is valid for incompressible flows, it is not realistic for compressible atmospheric flows observed at a kilometer order scale. However, based on experiments, authors proposed to apply directly this model to the image observations (Anonymous) or to the inverse of the image intensities (Zhou et al., 2000). Recently, under the assumption of negligible vertical wind, the model of Eq. 2 has been applied to pressure difference maps approximating the density integrals (Anonymous).

The formulations of Eq.1 and Eq.2 can not be used alone, as they provide only one equation for two unknowns at each spatio-temporal locations $(\mathbf{s},t)$, with therefore a one dimensional family of solutions in general. In order to remove this ambiguity and robustify the estimation, the most common assumption consists to enforce a spatial local coherence. The latter can explicitly be expressed as a regularity prior in a globalized smoothing scheme. Within this scheme, spatial dependencies are modeled on the complete image domain and thus robustness to noise and low contrasted observations is enhanced. More precisely, the motion estimation problem is defined as the global minimization of an energy function composed of two components :

$$J(\mathbf{v},I)=J_d(\mathbf{v},I)+\alpha J_r(\mathbf{v}) \tag{3}$$

The first component $J_d(\mathbf{v},I)$ called the data term, expresses the constraint linking unknowns to observations while the second component $J_r(\mathbf{v})$, called the regularization term, enforces the solution to follow some smoothness properties. In the previous expression, $\alpha>0$ denotes a parameter controlling the balance between the smoothness and the global adequacy to the observation model. In this framework, Horn and Schunck (Horn and Schunck, 1981) first introduced a data term related to the OFC equation and a first-order regularization of the two spatial components $u$ and $v$ of velocity field $\mathbf{v}$. In the case of transmittance imagery of fluid flows, $I=\int\rho dz$, and using the previously defined ICE model (Eq.2) leads to the functional :

$$J_d(\mathbf{v},I)=\int_\Omega\left(I_t(\mathbf{s})+\mathbf{v}(\mathbf{s})\cdot\nabla I(\mathbf{s})+I(\mathbf{s})\mathrm{div}\mathbf{v}(\mathbf{s})\right)^2 d\mathbf{s} \tag{4}$$

where $\Omega$ denotes the image domain.
Moreover, it can be demonstrated that a first order

regularization is not adapted as it favors the estimation of velocity fields with low divergence and low vorticity. A second order regularization on the vorticity and the divergence of the defined motion field can advantageously be considered as proposed in (Anonymous)(Suter, 1994)(Anonymous) :

$$J_r(\mathbf{v}) = \int_\Omega \| \nabla curl\mathbf{v}(\mathbf{s}) \|^2 + \| \nabla \mathrm{div}\mathbf{v}(\mathbf{s}) \|^2 \, d\mathbf{s} \qquad (5)$$

Instead of relying on a $L^2$ norm, robust penalty function $\phi_d$ may be introduced in the data term for attenuating the effect of observations deviating significantly from the ICE constraint (Black and Anandan, 1996). Similarly, a robust penalty function $\phi_r$ can be used if one wants to handle implicitly the spatial discontinuities of the vorticity and divergence maps. In the image plan, these discontinuities are nevertheless difficult to relate to abrupt variations of clouds height. Moreover, the robust approach does not allow points of unconnected regions, which belong to a same layer, to interact during the motion estimation process.

# 3 MODELING A DYNAMICAL STACK OF LAYERS

## 3.1 Integrated Continuity Equation for 3D Winds

Interesting models for 3D compressible atmospheric motion observed through image sequences may be derived by integrating the 3D continuity equation expressed in the isobaric coordinate system $(x,y,p)$. In comparison to standard altimetric coordinates, isobaric coordinates are advantageous : they enable to handle in a simple manner the compressibility of atmospheric flows while dealing directly with pressure quantities, which will be used as observations in this paper. In this coordinate system, the pressure function $p$ acts as a vertical coordinate. Let us denote the horizontal wind components by $\mathbf{v} = (u,v)$ and the vertical wind in isobaric coordinates by $\omega$. The 3D continuity equation reads (Holton, 1992) :

$$-\frac{\partial \omega}{\partial p} = \left(\frac{\partial u}{\partial x} + \frac{\partial v}{\partial y}\right)_p \qquad (6)$$

By defining now two altimetric surfaces $s^k$ and $s^{k+1}$ with $p(s^k) > p(s^{k+1})$ related to a pressure difference function $\delta p^k$ and a pressure-average horizontal wind field $\mathbf{v}^k$

$$\begin{aligned} \delta p^k &= p(s^k) - p(s^{k+1}) \\ \mathbf{v}^k &= \frac{1}{\delta p^k} \int_{p(s^{k+1})}^{p(s^k)} \mathbf{v} dp \end{aligned} \qquad (7)$$

we have demonstrated in appendix I that the vertical integration of Eq.6 in the altimetric interval $[s^k, s^{k+1}]$ yields under certain conditions to the following 3D-ICE model:

$$g\rho(s^k)\mathrm{w}(s^k) - g\rho(s^{k+1})\mathrm{w}(s^{k+1}) = \frac{d\delta p^k}{dt} + \delta p^k \mathrm{div}(\mathbf{v}^k) \qquad (8)$$

where $g$ and w denote the gravity constant and the vertical wind in the standard altimetric coordinate system $(x,y,z)$. Note that this model appears to be a generalization of the so called *kinematic method* applied in meteorology for the recovery of vertical motion (Holton, 1992). Indeed, by neglecting the first term on the right hand side of Eq.8, vertical motion can be expressed as :

$$\mathrm{w}(s^{k+1}) = \frac{\rho(s^k)\mathrm{w}(s^k)}{\rho(s^{k+1})} - \frac{\delta p^k}{g\rho(s^{k+1})}\mathrm{div}(\mathbf{v}^k), \qquad (9)$$

which corresponds exactly to the *kinematic* estimate. Note also that the ICE model (Eq.2) can be recovered when vertical motion is neglected and for an atmosphere in hydrostatic equilibrium ($\delta p = -g\int \rho dz$). On the right side of the 3D-ICE, vertical motion w appears only on the integration boundaries, while on the left side, pressure-average horizontal motion $\mathbf{v}^k$ appears within a standard optical flow expression compensated by a divergence correcting term. Thus, for pressure difference observations on layer boundaries, the 3D-ICE constitutes a possible 3D estimation model.

## 3.2 Layer Decomposition

The layering of atmospheric flow in the troposphere is valid in the limit of horizontal scales much greater than the vertical scale height, thus roughly for horizontal scales greater than 100 km. It is thus impossible to guarantee to truly characterize a layered atmosphere with a local analysis performed in the vicinity of a pixel characterizing a kilometer order scale. Nevertheless, one can still decompose the 3D space into elements of variable thickness, where only sufficiently thin regions of such elements may really correspond to common layers. Analysis based on such a decomposition presents the main advantage of operating at different atmospheric pressure ranges and avoids the mix of heterogeneous observations.

Let us present the 3D space decomposition that we chose for the definition of the layers. The $k$-th layer corresponds to the volume lying in between an upper surface $s^{k+1}$ and a lower surface $s^k$. These surfaces $s^j$ are defined by the height of top of clouds belonging to the $j$-th layer. They are thus defined only in areas where there exists clouds belonging to the $j$-th

layer, and remains undefined elsewhere. The membership of top of clouds to the different layers is determined by cloud classification maps. Such classifications which are based on thresholds of top of cloud pressure, are routinely provided by the EUMETSAT consortium, the European agency which supplies the METEOSAT satellite data.

### 3.3 Sparse Pressure Difference Observations

Top of cloud pressure images are also routinely provided by the EUMETSAT consortium. They are derived from a radiative transfer model using ancillary data obtained by analysis or short term forecasts (Lutz, 1999).

We denote by $C^k$ the class corresponding to the $k$-th layer. Note that the top of cloud pressure image denoted by $p_{\bigcup}$ is composed of segments of top of cloud pressure functions $p(s^{k+1})$ related to the different layers. That is to say : $p_{\bigcup} = \{\bigcup_k p(s^{k+1},\mathbf{s});\ \mathbf{s} \in C^k\}$. Thus, pressure images of top of clouds are used to constitute sparse pressure maps of the layer upper boundaries $p(s^{k+1})$. As in satellite images, clouds lower boundaries are always occluded, we coarsely approximate the missing pressure observations $p(s^k)$ by an average pressure value $\overline{p}^k$ observed on top of clouds of the layer underneath. Finally, for the $k$-th layer, we define observations $h^k$ as pressure differences :

$$\overline{p}^k - p_{\bigcup} = h^k \begin{cases} = \delta p^k(\mathbf{s}) & if \quad \mathbf{s} \in C^k \\ \neq \delta p^k(\mathbf{s}) & if \quad \mathbf{s} \in \bar{C}^k, \end{cases} \tag{10}$$

### 3.4 Layer Interacting Model

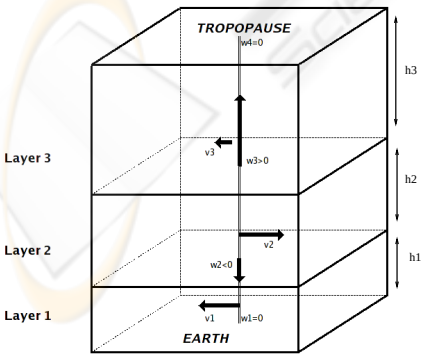


Figure 1: Scheme of three interacting layers defined at a given pixel location. The set of unknowns associated to the corresponding 3D-ICE model is $\{\mathbf{v}^1, w^2, \mathbf{v}^2, w^3, \mathbf{v}^3\}$. For the enhancement of the visual representation, pressure difference $h^k$ have been identified here to altimetric heights.

Eq.8 is thus valid for image observations $h^k$ related to the $k$-th layer on the spatial sub-domain $C^k$:

$$\frac{d(h^k)}{dt} + h^k \nabla \cdot \mathbf{v}^k = g(\rho^k \mathrm{w}^k - \rho^{k+1} \mathrm{w}^{k+1}) \tag{11}$$

where for clarity we have simplified notations $\rho(s^k)$ and $w(s^k)$ into $\rho^k$ and $w^k$. Density maps $\rho^k$ are fixed to a mean density value, which is computed according to the mean pressures $\overline{p}^k$ using the approximation : $\rho^k \approx p_0/(RT_0)(\overline{p}^k/p_0)^{(\gamma R)/g+1}$, where $p_0$, $T_0$, $\gamma$ and $R$ denote physical constants (Holton, 1992).

Integrating in time differential equation 11 along the horizontal trajectories and applying the variation of the constant tecnhique for the second member, we obtain a time-integrated form :

$$\tilde{h}^k e^{\mathrm{div}\mathbf{v}^k} - h^k = g\Delta t \frac{\rho^k \mathrm{w}^k - \rho^{k+1} \mathrm{w}^{k+1}}{\mathrm{div}\mathbf{v}^k} (e^{\mathrm{div}\mathbf{v}^k} - 1) \tag{12}$$

where the motion-compensated image $h^k(\mathbf{s}+\mathbf{v}^k, t+\Delta t)$ has been denoted for convenience by $\tilde{h}^k$ and where $\Delta t$ denotes the time interval expressed in seconds between two consecutive images.

For the lowest layer, the Earth boundary condition implies : $\mathrm{w}^1 = 0$. Let $K$ denote the index of the highest layer. Another boundary conditions may be given for the highest layer by the reasonable assumption that vertical wind can be neglected at the tropopause which acts like a cover : $\mathrm{w}^{K+1} = 0$. Thus, as the vertical wind present on the upper bound of the $k$-th layer is identical to the one present on the lower bound of the $(k+1)$-th layer, we have the following two sets of unknowns : $\{\mathbf{v}^k : k \in [1,K]\}$ and $\{\mathrm{w}^k : k \in [2,K]\}$. The vertical wind unknowns act as variables materializing horizontal wind interactions between adjacent layers. Fig.1 schematizes an example of three interacting layers associated to a set of unknowns, according to the 3D-ICE model.

## 4 3D WIND ESTIMATION

### 4.1 Dedicated Robust Estimator

Since outside the class $C^k$, $h^k$ defined in Eq.10 is not relevant of the $k$-th layer, we introduce a masking operator to remove unreliable observations by saturation of a robust penalty function $\phi_d$. More explicitly, we denote by $\mathbb{I}_{C^k}$ the operator which is identity if pixel belong to the class, and which returns a fixed value out of the range taken by $h^k$ otherwise. Thus, applying this new masking operator in Eq.12, we obtain for the $k$-th layer the robust data term $J_d(\mathbf{v}^k, \mathrm{w}^k, \mathrm{w}^{k+1}, h^k) =$

$$\int_\Omega \phi_d \big[\tilde{h}^k(\mathbf{s}) \exp\{\mathrm{div}\mathbf{v}^k(\mathbf{s})\} - \mathbb{I}_{C^k}(h^k(\mathbf{s})) + g\Delta t \frac{\rho^k \mathrm{w}^k(\mathbf{s}) - \rho^{k+1} \mathrm{w}^{k+1}(\mathbf{s})}{\mathrm{div}\mathbf{v}^k(\mathbf{s})} (1 - \exp\{\mathrm{div}\mathbf{v}^k(\mathbf{s})\})\big] d\mathbf{s} \tag{13}$$

A second order div-curl regularizer has been chosen to constrain spatial smoothness of horizontal wind fields. The latter was combined with a first order regularizer enforcing regions of homogeneous vertical winds. Note that we have restricted the regularizer for vertical wind to be a first order one, as 3D divergence and 3D vorticity vectors are inaccessible in a layered model. The regularization term for the $k$-th layer has been thus defined as $J_r(\mathbf{v}^k, \mathrm{w}^k) =$

$$\int_\Omega \alpha(\| \nabla curl \mathbf{v}^k(\mathbf{s}) \|^2 + \| \nabla \mathrm{div} \mathbf{v}^k(\mathbf{s}) \|^2) + \beta \| \nabla \mathrm{w}^k(\mathbf{s}) \|^2 d\mathbf{s}, \quad (14)$$

where $\beta > 0$ denotes a positive parameter. A Leclerc M-estimator has been chosen for $\phi_d$ for its advantageous minimization properties (Holland and Welsch, 1977). The masking procedure together with the use of this robust penalty function on the data term allows discarding implicitly the erroneous observations from the estimation process. It is important to outline that, for the $k$-th layer, the method provides estimates on all point $s$ of the image domain $\Omega$. Areas outside the cloud class $C^k$ correspond to 3D interpolated wind fields.

## 4.2 Large Horizontal Displacements

One major problem with the differential formulation of Eq.11 is the estimation of large displacements. However, on the opposite of the integrated form of Eq.12 which is valid for high amplitude displacements, this formulation presents the advantage to be linear. A standard approach for tackling the non-linear data term consists to apply successive linearizations around a current estimate and to warp a multiresolution representation of the data accordingly. This approach relies on an image pyramid, constructed by successive low-pass filtering and down sampling of the original images. A large displacement field $\tilde{\mathbf{v}}$ is first estimated at coarse resolution where motion amplitude should be sufficiently reduced in order to make the initial differential data model valid. Then, the estimation is refined through an incremental fields $\mathbf{v}'$ while going down the pyramid (Bergen et al., 1992). The latter are estimated within a linear scheme by minimizing linearized motion-compensated functionals : for the decomposition $\mathbf{v}^k = \tilde{\mathbf{v}} + \mathbf{v}'$, Eq.13 is linearized around $\tilde{\mathbf{v}}$ and yields to a motion-compensated linear formulation of the data term. Let us denote by $\tilde{\zeta}^k$ the coarse scale divergence estimate $\mathrm{div}\tilde{\mathbf{v}}$ and omit for sake of clarity point coordinates $\mathbf{s}$ in the integrals. For the $k$-th layer, the linearized data term reads $J_d(\mathbf{v}^k, \mathrm{w}^k, \mathrm{w}^{k+1}, h^k) =$

$$\int_\Omega \phi_d \{ e^{\tilde{\zeta}^k} ([\tilde{h}^k \nabla \tilde{\zeta}^k + \nabla \tilde{h}^k]^T \mathbf{v}' + \tilde{h}^k) - \mathbb{I}_{C^k}(h^k) + g\Delta t\, f(\tilde{\zeta}^k, \mathrm{w}^k, \mathrm{w}^{k+1}) \} d\mathbf{s} \quad (15)$$

where if $\tilde{\zeta}^k \neq 0$, $f(\tilde{\zeta}^k, \mathrm{w}^k, \mathrm{w}^{k+1}) =$

$$\frac{\rho^k \mathrm{w}^k - \rho^{k+1} \mathrm{w}^{k+1}}{\tilde{\zeta}^k} \left(1 - e^{\tilde{\zeta}^k} + \mathbf{v}' \nabla \tilde{\zeta}^k \left(\frac{e^{\tilde{\zeta}^k} - 1}{\tilde{\zeta}^k} - e^{\tilde{\zeta}^k}\right)\right)$$

and if $\tilde{\zeta}^k = 0$, $f(\tilde{\zeta}^k, \mathrm{w}^k, \mathrm{w}^{k+1}) = \rho^{k+1} \mathrm{w}^{k+1} - \rho^k \mathrm{w}^k$

## 4.3 Minimization Issues

In the proposed optimization scheme, we chose to minimize a discretize version of functionals of Eq. 15 and Eq. 14. Let us denote by $z^k$ the robust weights associated to the semi-quadratic penalty function related to the data term. Minimization is done by alternatively solving large systems for unknowns $\mathbf{v}^k$, $\mathrm{w}^k$ and $z^k$ through a multigrid Gauss-Seidel solver. More explicitly, all variables are first initialized to zero. A global optimization procedure is then successively operated at each level of the multiresolution pyramid. This procedure first performs in a multigrid optimization strategy, the minimization with respect to $\mathbf{v}^k$ of a linearized functional composed of the data term defined in Eq.15 and of the second order smoothness term defined in Eq.14. As variables $\{\mathrm{w}^k\}$ and $\{z^k\}$ are first frozen, this first step can be performed independently for each layer level $k \in [1, K]$. Once the minima have been reached, in a second step, fixing variables $\{\mathbf{v}^k\}$ and $\{z^k\}$, the same functional is minimized with respect to each $\mathrm{w}^k, k \in [2, K]$.

Note that vertical wind $\mathrm{w}^k$ is estimated considering variables related to the layer above the boundary $\{\mathrm{w}^{k+1}, h^k, \tilde{h}^k, \mathbf{v}^k, z^k\}$ and the layer underneath the boundary $\{\mathrm{w}^{k-1}, h^{k-1}, \tilde{h}^{k-1}, \mathbf{v}^{k-1}, z^{k-1}\}$. Finally, in a last step for each pixel locations and for each $k \in [1, K]$, the robust weights $z^k$ are in turn updated while variables $\{\mathbf{v}^k\}$ and $\{\mathrm{w}^k\}$ are kept fixed. The three previous minimization steps are iterated until a global convergence criterion is reached, that is to say until the variation of the estimated solution between two consecutive iterations becomes sufficiently small.

It is important to point out that the proposed 3D estimation methodology does not increase much the complexity of the original non-linear horizontal motion estimation problem. Indeed, given horizontal motion, the vertical wind estimation constitutes a linear quadratic problem which can be efficiently solved.

# 5 EXPERIMENTAL EVALUATION

## 5.1 Synthetic Image Sequence

For an exhaustive evaluation, we have relied on a simulated flow of an atmosphere decomposed into $K = 3$

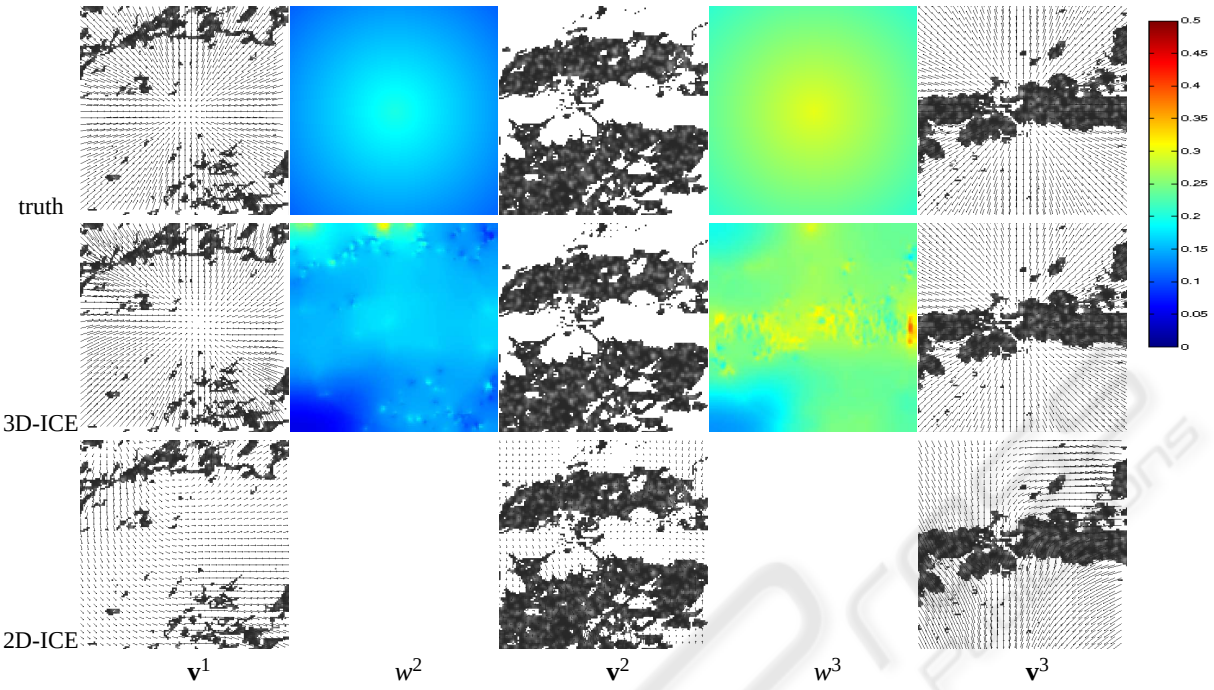


Figure 2: Recovery of horizontal $\{\mathbf{v}^1,\mathbf{v}^2,\mathbf{v}^3\}$ and vertical $\{w^2,w^3\}$ wind fields. Simulated 3D winds ($1^{st}$ line). Horizontal winds related to the high (left), the medium (middle) and the low (right) layer are superimposed on the cloud pressure difference observations. Horizontal motion estimated with the 3D ICE model ($2^{nd}$ line) have been compared to results obtained with a 2D version of the model ($3^{rd}$ line).

layers corresponding to low, medium and high clouds. The resulting synthetic images have been chosen to simulate a layered atmosphere contracting itself at its basis, driven by ascendant winds, and expanding itself at its top. Let us describe the 3D motion simulation. A real cloud classification map (used in the next experiment) has been employed to dissociate the layers, and to assign them to different image regions $C^k$. Thus, for each layers $k$, a sparse image $h^k(t)$ of 128 by 128 pixels has been generated, representative of cloud pressure difference measurements on the assigned regions $C^k$ and of a fixed saturation value on the complementary domain. A textured image of mean 600 hPa and with a standard deviation of 100 hPa has been used to simulate cloud pressure difference values. The three resulting images are presented in figure 2. An horizontal motion $\mathbf{v}^1$ issued from a divergent sink has been imposed to the lower layer, while on the middle layer no horizontal winds $\mathbf{v}^2 = 0$ has been considered. On the higher layer, a motion $\mathbf{v}^3$ issued from a divergent source has been applied. The latter sink and source possess a decreasing influence while going away from the center of the image to its boundaries (motion amplitudes ranges in the interval $\sim 0-1.25$ pixel per frame, that is $\sim 0-4\,m.s^{-1}$). Non-uniform vertical winds of strength $w^2 \in [0.1,0.2]\,m.s^{-1}$ and $w^3 \in [0.2,0.3]\,m.s^{-1}$ have been simulated on the boundaries shared respectively by the lower and the medium layers, and by the medium and the high layers respectively. The latter horizontal and vertical winds have been used to deform, according to the time integrated 3D-ICE model (Eq.12), image observations $[h^1(t),h^2(t),h^3(t)]$ in order to generate propagated images $[h^1(t+\Delta t),h^2(t+\Delta t),h^3(t+\Delta t)]$ with $\Delta t$ =900 seconds.

| | | Barron's error (degree) | Speed bias (pixel) | RMSE (m/s) |
|---|---|---|---|---|
| 3D-ICE | $w^3$ | | | 0.027 |
| | $w^2$ | | | 0.028 |
| | $\mathbf{v}^3$ | 6.426 | 0.099 | |
| | $\mathbf{v}^2$ | 0.138 | 0.002 | |
| | $\mathbf{v}^1$ | 3.566 | 0.058 | |
| 2D-ICE | $\mathbf{v}^3$ | 29.608 | 0.210 | |
| | $\mathbf{v}^2$ | 6.331 | 0.112 | |
| | $\mathbf{v}^1$ | 38.276 | 0.161 | |

Figure 3: Numerical evaluation. Barron angular error and speed bias on horizontal winds $\{\mathbf{v}^1,\mathbf{v}^2,\mathbf{v}^3\}$ and RMSE on vertical wind $\{w^2,w^3\}$ provided by the 3D-ICE model. Comparison with horizontal winds produced by a 2D version of the model.

Horizontal and vertical winds which have been retrieved with the 3D estimator can be visualized in figure 2. For the three layer levels, vertical and horizontal winds are accurately estimated in cloudy regions. The estimator accuracy is evaluated in table 3, using for horizontal wind the Barron angular error (Barron et al., 1994) and the speed bias, and for vertical wind the Root Mean Square Error (RMSE). In observations free areas, vertical and horizontal winds appear to be consistent with the divergent and ascendant motions. Note that in the latter regions, the estimator acts as a 3D wind extrapolator. Moreover, it can be noticed that the proposed layer interacting model increases significantly the estimation performances. In particular, the convergent motion of the lower layer is well characterized although only very few observations are available. For comparison purpose we have run on this sequence the same estimator imposing a zero value to the unknown vertical components. This comes to use the 2D layered data model as proposed in (Anonymous). As a result, this estimator calculates independent horizontal winds for the three different layers in the very same numerical implementation setup as for the 3D wind estimator. Results which are presented in figure 2 and in table 3 show that the latter estimator completely fails to accurately characterize horizontal motion. This demonstrates that, although vertical wind ($\sim 0.1-0.3 m.s.^{-1}$) is weak compared to horizontal motion ($\sim 0-4 m.s.^{-1}$), its influence can not be neglected in the estimation process. As evaluated in table 3, a 3D data model clearly improves the results in such a situation.

### 5.2 Satellite Image Sequence

We then turned to qualitative evaluations on a METEOSAT Second Generation meteorological sequence of 4 images acquired at a rate of an image every 15 minutes, with a spatial resolution of 3 kilometers at the center of the whole Earth image disk. The images of 512 by 200 pixels cover an area over the Gulf Guinea. The images are EUMETSAT top of cloud pressure observations which are associated to top of cloud classifications (Lutz, 1999). According to section 3.3, pressure images and classifications maps have been used to derive pressure difference image segments for 3 broad layers, at low, intermediate and high altitude. Figure 4 displays the pressure difference images related to the higher layer, together with the 3D estimated wind fields. One can visualize here large convective systems. They are characterized by strong ascendant flows which are smoothly reversed after bursting while reaching the tropopause cover. Such scenarios have been correctly estimated as shown in figure 4. Furthermore, let us remark that the time-consistency and the correct range of wind values estimated are a testimony of the stability of the 3D estimation method.

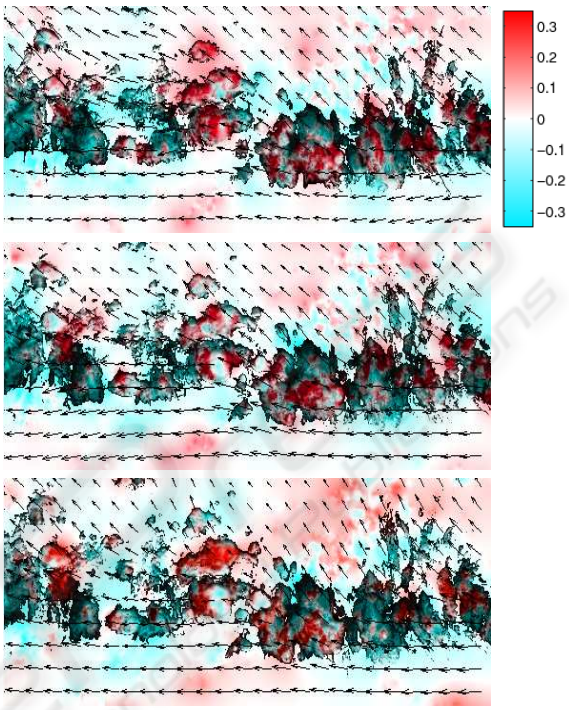


Figure 4: Estimation of 3D wind in atmospheric convective systems. Cloud pressure difference images of the highest layer at 3 consecutive times (from top to bottom). Estimated horizontal wind vectors which have been plotted on the images range in the interval $[0,10] m.s.^{-1}$. Retrieved vertical wind maps on the highest layer lower boundary have been superimposed on the pressure difference images with a shaded red color for ascendant motion and a shaded blue color for descendant motion. Vertical wind ranges in the interval $[-0.5,0.5] m.s.^{-1}$.

## 6 CONCLUSIONS

In this paper, we have presented a motion estimation method solving for the first time the complex problem of 3D winds field recovery from satellite image sequences. In order to manage incomplete observations, physical knowledge on 3D mass exchanges between atmospheric layers have been introduced within an optical flow scheme.

The estimator is based on a functional minimization. The data term relies on the 3D-ICE model which describes the dynamics of an interacting stack of atmospheric layers. The 3D-ICE model applies on a set of sparse pressure difference images related to the different atmospheric layers. A method is proposed

to reconstruct such observations from satellite top of cloud pressure images and classification maps. To overcome the problem of sparse observations, a robust estimator is introduced in the data term. The data term is combined to a regularizers preserving bi-dimensional divergent and vorticity structures of the three-dimensional flow and enforcing regions of homogeneous vertical winds.

An evaluation first performed on a synthetic image sequence, and latter on a METEOSAT pressure image sequences demonstrate the stability and the efficiency of the method even in the difficult case of very sparse image observations.

# REFERENCES


Barron, J., Fleet, D., and Beauchemin, S. (1994). Performance of optical flow techniques. *Int. J. Computer Vision*, 12(1):43–77.

Bergen, J., Burt, P., Hingorani, R., and Peleg, S. (1992). A three-frame algorithm for estimating two-component image motion. *IEEE Trans. Pattern Anal. Machine Intell.*, 14(9):886–895.

Black, M. and Anandan, P. (1996). The robust estimation of multiple motions: Parametric and piecewise-smooth flow fields. *Computer Vision and Image Understanding*, 63(1):75–104.

Fitzpatrick, J. (1988). The existence of geometrical density-image transformations corresponding to object motion. *Comput. Vision, Graphics, Image Proc.*, 44(2):155–174.

Holland, P. and Welsch, R. (1977). Robust regression using iteratively reweighted least-squares. *Commun. Statis.-Theor. Meth.*, A6(9):813–827.

Holton, J. (1992). *An introduction to dynamic meteorology*. Academic press.

Horn, B. and Schunck, B. (1981). Determining optical flow. *Artificial Intelligence*, 17:185–203.

Larsen, R., Conradsen, K., and Ersboll, B. (1998). Estimation of dense image flow fields in fluids. *IEEE trans. on Geoscience and Remote sensing*, 36(1):256–264.

Leese, J., Novack, C., and Clark, B. (1971). An automated technique for obtained cloud motion from geosynchronous satellite data using cross correlation. *Journal of applied meteorology*, 10:118–132.

Lutz, H. (1999). Cloud processing for meteosat second generation. Technical report, European Organisation for the Exploitation of Meteorological Satellites (EUMETSAT), Available at : http://www.eumetsat.de.

Suter, D. (1994). Motion estimation and vector splines. In *Proc. Conf. Comp. Vision Pattern Rec.*, pages 939–942, Seattle, USA.

Zhou, L., Kambhamettu, C., and Goldgof, D. (2000). Fluid structure and motion analysis from multi-spectrum 2d cloud images sequences. In *Proc. Conf. Comp. Vision Pattern Rec.*, volume 2, pages 744–751, USA.


# APPENDIX I

## Vertical Integration of the Continuity Equation

For compressible fluids, the continuity equation in the $(x,y,p)$ coordinates system reads:

$$-\frac{\partial \omega}{\partial p} = \left(\frac{\partial u}{\partial x} + \frac{\partial v}{\partial y}\right)_p \tag{16}$$

Let us denote by $s^k$ and $s^{k+1}$ altimetric surfaces with $p(s^k) > p(s^{k+1})$. According to the Leibnitz formula, integrating Eq.16 in the varying pressure interval $[p(s^{k+1}), p(s^k)]$ yields to :

$$\begin{aligned}[\omega]_{s^k}^{s^{k+1}} &= \mathrm{div}\Big|_p \int_{p(s^{k+1})}^{p(s^k)} \mathbf{v} dp - \mathbf{v}(s^k).\nabla_{xy}(p(s^k))\Big|_{s^k} \\ &+ \mathbf{v}(s^{k+1}).\nabla_{xy}(p(s^{k+1}))\Big|_{s^{k+1}}\end{aligned} \tag{17}$$

Moreover, expanding $\omega$ in the $(x,y,z)$ coordinates system and using the hydrostatic assumption ($\frac{\partial p}{\partial z} = -\rho g$) yields to

$$\omega = \frac{dp}{dt} = \frac{\partial p}{\partial t} + \mathbf{v}\cdot\nabla_{xy}(p) - \mathrm{w}\rho g, \tag{18}$$

where w is the vertical velocity in $z$ coordinates and where we have introduced the density functions $\rho$ and the gravity constant $g$. Assuming that the surface $s^k$ is flat in the vicinity of a pixel, by merging Eq. 17 and Eq. 18, we obtain

$$g[\rho \mathrm{w}]_{s^{k+1}}^{s^k} + \frac{\partial (p(s^{k+1}) - p(s^k))}{\partial t}\Big|_{I_s} \simeq \mathrm{div}\Big|_p \int_{p(s^{k+1})}^{p(s^k)} \mathbf{v} dp \tag{19}$$

where we have denoted by $I_s$ the altimetric interval between surfaces $s^k$ and $s^{k+1}$. Let us now define the following quantities :

$$\begin{aligned}\delta p^k &= p(s^k) - p(s^{k+1}) \\ \mathbf{v}^k &= \frac{1}{\delta p^k}\int_{p(s^{k+1})}^{p(s^k)} \mathbf{v} dp\end{aligned} \tag{20}$$

Considering the reasonable approximation $\mathrm{div}(\mathbf{v}^k)\Big|_p \simeq \mathrm{div}(\mathbf{v}^k)\Big|_{I_s}$, we can then rewrite Eq. 19 as

$$\begin{aligned}g\rho(s^k)\mathrm{w}(s^k) - g\rho(s^{k+1})\mathrm{w}(s^{k+1}) \simeq \\ \frac{\partial \delta p^k}{\partial t}\Big|_{I_s} + \mathbf{v}^k\cdot\nabla_{xy}(\delta p^k)\Big|_{I_s} + \delta p^k \mathrm{div}(\mathbf{v}^k)\Big|_{I_s}\end{aligned} \tag{21}$$

Simplifying notations of operators defined for the altimetric interval $I_s$, we obtain the relation :

$$g\rho(s^k)\mathrm{w}(s^k) - g\rho(s^{k+1})\mathrm{w}(s^{k+1}) \simeq \frac{d\delta p^k}{dt} + \delta p^k \mathrm{div}(\mathbf{v}^k), \tag{22}$$

which consitutes a proper image-adapted model for observations $\delta p^k$ related to a layer defined in the interval $I_s$.